

Banner appropriate to article type will appear here in typeset article

Adaptive near-contact repulsion in conservative Allen–Cahn phase-field lattice Boltzmann multiphase model

Andrea Montessori¹†, Maria Rosa Lisboa², Marco Lauricella³ and Sauro Succi^{4,5}

¹Department of Civil, Computer Science and Aeronautical Technologies Engineering, Roma Tre University, Via Vito Volterra, Rome, 00146, Italy

²Pontifícia Universidade Católica do Paraná, Rua Imaculada Conceição, 1155, Curitiba, 80215-901, Brazil

³Istituto per le Applicazioni del Calcolo, Consiglio Nazionale delle Ricerche, Via dei Taurini 19, Rome, 00185, Italy

⁴Center for Life Nano- & Neuro-Science, Fondazione Istituto Italiano di Tecnologia, Viale Regina Elena 291, Rome, 00161, Italy

⁵PoreLab, Department of Physics, Norwegian University of Science and Technology, 7491 Trondheim, Norway

(Received xx; revised xx; accepted xx)

Unresolved thin-film dynamics often causes spurious coalescence in diffuse-interface simulations of multiphase flows. We address this issue by introducing a fully local repulsive near-contact flux in a conservative Allen–Cahn phase-field model coupled to lattice Boltzmann hydrodynamics. The interaction activates only for oppositely oriented nearby interfaces, with a strength that self-adjusts based upon an analytical estimate of the local film thickness extracted from the phase field. The resulting method circumvents nonlocal geometric procedures, preserves computational efficiency, and is well suited to massively parallel implementations. Tests on collision benchmarks and three-dimensional bubble swarms demonstrate robust suppression of artificial merging and physically consistent near-contact dynamics.

1. Introduction

Multiphase flows are central to a broad range of natural phenomena, environmental processes, engineering and life-science applications as well. They play a key role in cloud physics Shaw (2003), aerosol transport Guha (2008), boiling and condensation Kharangate & Mudawar (2017), emulsification Bogdan *et al.* (2022); Håkansson (2019), bubble-driven mixing Risso (2018), microfluidics Sattari *et al.* (2020), porous-media transport Miller *et al.* (1998) and energy-related technologies such as carbon sequestration and subsurface storage Ringrose *et al.* (2021). In all these settings, the dynamics of interfaces controls momentum exchange, mass transport, topology changes, and ultimately the large-scale behavior of the system. A predictive description of multiphase flows is, therefore, of major importance both for advancing fundamental understanding and for enabling the rational design of technological processes.

† Email address for correspondence: andrea.montessori@uniroma3.it

However, numerical investigation of such flows remains highly challenging Tiribocchi *et al.* (2025); Balachandar & Eaton (2010); Subramaniam (2020). The main difficulty lies in the need to accurately capture the interplay between physical mechanisms of different nature that act on widely separated spatial and temporal scales Subramaniam (2020). At the macroscopic level, inertia, viscous stresses, capillary forces, and buoyancy govern the global flow evolution. At the same time, many crucial events are controlled by localized interfacial processes occurring over much smaller scales, such as thin-film drainage, interface deformation, rupture, and near-contact interactions Craster & Matar (2009); Dai *et al.* (2008); Boinovich & Emelyanenko (2002); Tirumkudulu & Russel (2004). These processes often determine whether two interfaces merge, rebound, slide past each other, or remain separated, thereby strongly affecting the overall evolution of the system. The resulting cross-scale coupling poses a major challenge for numerical models, especially in three-dimensional simulations and in the presence of large density and viscosity contrasts.

These considerations motivate the development of accurate, high-fidelity, and computationally efficient numerical methods capable of resolving interface dynamics while also accounting for physical effects that cannot be directly represented within the standard continuum description based on the Navier-Stokes equations alone Tiribocchi *et al.* (2025). Although classical hydrodynamic models provide the correct large-scale framework, they are not sufficient, by themselves, to describe unresolved interfacial physics arising at scales below the numerical grid resolution, particularly during near-contact events. As a result, there is a decided need for computational approaches that combine robust mesoscale hydrodynamic solvers, accurate interface-capturing formulations, and suitable closures for subgrid interfacial phenomena. Moreover, such approaches must also retain a high degree of locality and algorithmic efficiency in order to remain viable for large-scale simulations on modern high-performance computing architectures Succi *et al.* (2019).

The aim of the present paper is to develop such a framework in the context of diffuse-interface multiphase flow modeling. More specifically, we introduce a repulsive near-contact flux Montessori *et al.* (2019) within a conservative Allen–Cahn phase-field formulation Jeong & Kim (2017) coupled to a lattice Boltzmann solver for the hydrodynamics Benzi *et al.* (1992); Krüger *et al.* (2017). The proposed model is designed to prevent spurious coalescence when two interfaces approach each other across an unresolved thin film, while preserving the locality, robustness, and computational efficiency of the underlying numerical method. The central idea is to account for unresolved near-contact physics through a short-range repulsive contribution that is activated only whenever two diffuse interfaces come sufficiently close and exhibit opposite orientation, namely in configurations compatible with the formation of an intervening liquid film. In this way, the model selectively targets those interfacial interactions for which standard diffuse-interface descriptions are most prone to artificial merging, while remaining inactive elsewhere and therefore minimally intrusive on the resolved hydrodynamics.

A distinctive feature of the proposed formulation is that the local film thickness is not obtained through explicit geometric reconstruction, ray tracing along interface normals, or other nonlocal procedures. Instead, it is estimated analytically and locally from the phase-field profile itself, thereby preserving the compact stencil and strict locality of the numerical scheme. This construction also endows the repulsive interaction with a self-tuning character: the magnitude of the near-contact flux is not prescribed as a fixed ad hoc correction, but adapts dynamically to the local degree of interface overlap and to the corresponding hydrodynamic tendency toward coalescence. As the drainage-driven approach between interfaces becomes stronger and the effective film thickness decreases, the repulsive contribution automatically intensifies, counteracting further collapse of the intervening layer; conversely, when the interfaces separate, the flux rapidly vanishes. The resulting mechanism provides a coarse-

grained but physically consistent closure of unresolved thin-film stabilization, capable of balancing the spurious attractive tendency induced by insufficient spatial resolution without introducing long-range artifacts or unnecessary distortion of the bulk flow.

Because the entire formulation is local, explicit and free of costly geometric operations, it is particularly well suited for thread-safe and massively parallel implementations Montessori *et al.* (2024); Lauricella *et al.* (2025b). This makes it especially attractive for large-scale three-dimensional simulations of complex interfacial flows, where many-body near-contact events occur frequently and where numerical efficiency is as critical as physical fidelity.

The paper is organized as follows. Section Methods presents the numerical methodology, including the hydrodynamic lattice Boltzmann solver, the conservative Allen–Cahn phase-field formulation, and the derivation and implementation of the repulsive near-contact flux. Section Results assesses the performance of the model through representative benchmark problems and application cases, highlighting its ability to capture collision dynamics and many-body interfacial interactions without spurious merging. Finally, in the Conclusions we summarize the main findings and discuss perspectives for future developments.

2. Methods

In three-dimensional multiphase flows, whether two deformable interfaces merge or rebound is often decided within the thin intervening film that forms at near-contact Qian & Law (1997); Orme (1997). Coalescence requires this film (gas or liquid, depending on the configuration) to drain down to a critical thickness at which rupture is triggered by short-range intermolecular attraction; conversely, if drainage is sufficiently slow, or if additional repulsive stresses stabilize the film Bergeron (1999), the interfaces can remain separated long enough for rebound to occur. Importantly, this transition does not rely exclusively on surfactant-mediated steric effects: experiments on binary droplet collisions Gunn (1965); Qian & Law (1997); Huang & Pan (2021) show that bouncing can appear or disappear in *clean* systems solely by changing droplet diameter and fluid properties, because these parameters control the characteristic minimum film thickness and the drainage dynamics in the interfacial gap.

Diffuse-interface (phase-field) models typically cannot resolve the nanometric scales associated with film drainage and rupture Li (2016). As a consequence, the interfacial gap may collapse prematurely and yield unphysical coalescence, even in regimes where real systems would bounce. To represent, at the mesoscopic level, the stabilizing action of unresolved thin-film physics (e.g. lubrication-induced delay, steric/electrostatic repulsion, and other short-range interfacial interactions), we augment the conservative Navier–Stokes equations with a *repulsive force* term that is activated only when two diffuse interfaces approach each other with opposite orientations Montessori *et al.* (2019). This near-contact interaction can be interpreted as a coarse-grained repulsive normal stress that effectively increases the time required for the film to reach the rupture threshold, thereby enabling controlled *frustration of coalescence* in interacting interfacial systems.

Unlike previous NCI approaches Montessori *et al.* (2019); Liu *et al.* (2025), the present formulation does not require ray tracing along the interface normal, in order to identify neighboring interfaces. Instead, it estimates the local separation distance analytically by exploiting the equilibrium profile of diffuse-interface models, improving computational efficiency and ensuring enhanced antisymmetric properties of the short-range interaction.

2.1. Coupled Recursive regularized Thread-safe lattice Boltzmann and finite-difference MUSCL scheme for Navier-Stokes Conservative Allen Cahn equations

We solve the hydrodynamics of the two-component system through a thread-safe lattice Boltzmann (LB) method, implemented in *accLB* Lauricella *et al.* (2025a); Montessori *et al.*

(2026) and coupled to an interface-capturing phase-field solver (described later). The LB solver is designed to (i) remain fully local on shared-memory architectures (GPU), thereby avoiding memory race conditions during streaming/collision, and (ii) improve stability at low viscosities through a third-order recursive regularization of non-equilibrium moments Montessori *et al.* (2024).

Hydrodynamic limit. In the low-Mach, small-Knudsen limit, the discrete kinetic dynamics recovers the variable-density, variable-viscosity Navier–Stokes equations Fakhari *et al.* (2017); Zu & He (2013)

$$\partial_t \rho + \nabla \cdot (\rho \mathbf{u}) = 0, \quad (2.1)$$

$$\partial_t (\rho \mathbf{u}) + \nabla \cdot (\rho \mathbf{u} \otimes \mathbf{u}) = -\nabla p + \nabla \cdot \left[\rho \nu \left(\nabla \mathbf{u} + (\nabla \mathbf{u})^T \right) \right] + \mathbf{F}_\sigma + \mathbf{F}_{\text{rep}} + \mathbf{F}_{\text{ext}}. \quad (2.2)$$

Here ρ is the mixture density, \mathbf{u} the velocity, ν the kinematic viscosity, and \mathbf{F}_σ is the capillary (surface-tension) force density. The term \mathbf{F}_{rep} denotes the near-contact repulsive contribution introduced in Sec. 2.2, while \mathbf{F}_{ext} collects possible external body forcings.

Discrete kinetic equation and thread-safe update. We consider a q -speed stencil (D3Q27) with discrete velocities $\{\mathbf{c}_i\}_{i=0}^{q-1}$, weights $\{w_i\}$, and lattice time step $\Delta t = 1$. The LB dynamics reads Krüger *et al.* (2017); Benzi *et al.* (1992)

$$f_i(\mathbf{x} + \mathbf{c}_i, t + 1) = f_i(\mathbf{x}, t) + \omega \left[f_i^{\text{c}q}(\mathbf{x}, t) - f_i(\mathbf{x}, t) \right] + S_i(\mathbf{x}, t), \quad (2.3)$$

where f_i are the populations, ω is the relaxation frequency, and S_i is a forcing source term Guo *et al.* (2002). The kinematic viscosity is linked to ω through

$$\nu = c_s^2 \left(\frac{1}{\omega} - \frac{1}{2} \right), \quad (2.4)$$

with c_s the lattice sound speed Succi (2018). Following the thread-safe paradigm, both the equilibrium and non-equilibrium parts are reconstructed from local macroscopic fields via a Hermite expansion (see below), so that each lattice node can be updated independently without reading/writing neighboring populations (single-pass streaming–collision, no flip-flop buffering). This eliminates race conditions on shared-memory parallel architectures.

Macroscopic fields. We employ the incompressible-pressure formulation Zu & He (2013) where the kinetic zeroth moment yields a dimensionless pressure-like field p^* , while the physical pressure is

$$p = \rho c_s^2 p^*. \quad (2.5)$$

The macroscopic fields are recovered as

$$p^*(\mathbf{x}, t) = \sum_i f_i(\mathbf{x}, t), \quad (2.6)$$

$$\mathbf{u}(\mathbf{x}, t) = \sum_i f_i(\mathbf{x}, t) \mathbf{c}_i + \frac{1}{2} \sum_i S_i(\mathbf{x}, t) \mathbf{c}_i. \quad (2.7)$$

The density ρ and viscosity ν are space-dependent and determined from the phase field (mixture law), which will be detailed together with the interface-transport equation in the next section.

Mixture properties and relaxation frequency. The local material properties are functions of the phase field $\phi \in [0, 1]$ (with $\phi = 0$ in the gas and $\phi = 1$ in the liquid). In the present work we interpolate the *dynamic* viscosity linearly as Fakhari *et al.* (2017)

$$\mu(\phi) = \mu_g + (\mu_\ell - \mu_g) \phi. \quad (2.8)$$

The kinematic viscosity then follows from $\nu(\phi) = \mu(\phi)/\rho(\phi)$, i.e.

$$\nu(\phi) = \frac{\mu_g + (\mu_\ell - \mu_g)\phi}{\rho(\phi)}. \quad (2.9)$$

Accordingly, the relaxation frequency is space-dependent and given by

$$\omega(\phi) = \left(\frac{1}{2} + \frac{\nu(\phi)}{c_s^2} \right)^{-1}, \quad \tau(\phi) = \omega(\phi)^{-1}. \quad (2.10)$$

The density field $\rho(\phi)$ is obtained from the phase-field mixture rule (reported together with the phase-field model in the next section), and is used consistently in the pressure relation $p = \rho c_s^2 p^*$.

Third-order equilibrium. The equilibria are obtained from a third-order (Mach-number) Hermite expansion Montessori *et al.* (2024, 2015); Malaspina (2015):

$$f_i^{\text{eq}} = w_i \left[p^* + \frac{\mathbf{c}_i \cdot \mathbf{u}}{c_s^2} + \frac{\mathcal{H}_i^{(2)} : (\mathbf{u} \otimes \mathbf{u})}{2c_s^4} + \frac{\mathcal{H}_i^{(3)} \vdots (\mathbf{u} \otimes \mathbf{u} \otimes \mathbf{u})}{6c_s^6} \right], \quad (2.11)$$

where “:” denotes double contraction between second-order tensors and “\vdots” the triple contraction between third-order tensors. The second- and third-order Hermite tensors are

$$\mathcal{H}_i^{(2)} = \mathbf{c}_i \otimes \mathbf{c}_i - c_s^2 \mathbf{I}, \quad (2.12)$$

$$\mathcal{H}_i^{(3)} = \mathbf{c}_i \otimes \mathbf{c}_i \otimes \mathbf{c}_i - c_s^2 \mathcal{S}(\mathbf{c}_i \otimes \mathbf{I}), \quad (2.13)$$

with \mathbf{I} the identity tensor and $\mathcal{S}(\cdot)$ the full symmetrization over index permutations (e.g. $\mathcal{S}(\mathbf{c} \otimes \mathbf{I}) = \mathbf{c} \otimes \mathbf{I} + \mathbf{I} \otimes \mathbf{c} + \dots$).

Recursive regularization of non-equilibrium populations. We decompose $f_i = f_i^{\text{eq}} + f_i^{\text{neq}}$ and reconstruct f_i^{neq} up to third order as

$$f_i^{\text{neq}} = w_i \left[\frac{\mathcal{H}_i^{(2)} : \mathbf{A}_{\text{neq}}^{(2)}}{2c_s^4} + \frac{\mathcal{H}_i^{(3)} \vdots \mathbf{A}_{\text{neq}}^{(3)}}{6c_s^6} \right], \quad (2.14)$$

where $\mathbf{A}_{\text{neq}}^{(2)}$ is the (symmetric) second-order non-equilibrium moment and $\mathbf{A}_{\text{neq}}^{(3)}$ is obtained via Hermite recursivity Szeg (1939). At the Navier–Stokes level, $\mathbf{A}_{\text{neq}}^{(2)}$ can be expressed in gradient form as

$$\mathbf{A}_{\text{neq}}^{(2)} = -\frac{1}{\omega c_s^2} \left[\nabla(\rho \mathbf{u}) + \nabla(\rho \mathbf{u})^T \right], \quad (2.15)$$

while the third-order tensor is obtained recursively as

$$\mathbf{A}_{\text{neq}}^{(3)} = \mathcal{S}(\mathbf{u} \otimes \mathbf{A}_{\text{neq}}^{(2)}). \quad (2.16)$$

In practice, the regularization acts as a projection of f_i^{neq} onto the Hermite subspace spanned by moments up to third order, filtering out higher-order ghost modes and improving robustness at low viscosity/high Reynolds number regimes.

Forcing scheme and multiphase force decomposition. Forcing is incorporated via the Guo source term Guo *et al.* (2002),

$$S_i = w_i \left[\frac{\mathbf{c}_i - \mathbf{u}}{c_s^2} + \frac{(\mathbf{c}_i \cdot \mathbf{u})}{c_s^4} \mathbf{c}_i \right] \cdot \mathbf{F}, \quad (2.17)$$

and implemented consistently with the trapezoidal rule by shifting the equilibria (equivalent to using $f_i^{\text{eq}} \leftarrow f_i^{\text{eq}} - \frac{1}{2}S_i$ in the collision operator).

For multiphase flows with strong density/viscosity inhomogeneities, we decompose Zu & He (2013)

$$\mathbf{F} = \mathbf{F}_\sigma + \mathbf{F}_p + \mathbf{F}_v + \mathbf{F}_{\text{rep}} + \mathbf{F}_{\text{ext}}. \quad (2.18)$$

The capillary contribution is expressed in chemical-potential form Jacqmin (1999),

$$\mathbf{F}_\sigma = \mu_\phi \nabla \phi, \quad (2.19)$$

where ϕ is the phase field and μ_ϕ its chemical potential (defined together with the phase-field model).

Because the pressure is given by $p = \rho c_s^2 p^*$, its gradient splits as $\nabla p = \rho c_s^2 \nabla p^* + p^* c_s^2 \nabla \rho$. The first term is embedded in the choice of equilibria (2.11), whereas the second term must be included explicitly as a correction force

$$\mathbf{F}_p = -p^* c_s^2 \nabla \rho. \quad (2.20)$$

Finally, in order to reproduce the variable-coefficient viscous operator in (2.2), an additional correction proportional to $\nabla \rho$ is introduced by exploiting the link between the second-order kinetic moment and the deviatoric stress Krüger *et al.* (2009). In compact tensor form, this reads:

$$\mathbf{F}_v = -\frac{\nu\omega}{c_s^2} \left[\sum_i (f_i - f_i^{\text{eq}}) (\mathbf{c}_i \otimes \mathbf{c}_i) \right] \cdot \nabla \rho, \quad (2.21)$$

where “ \cdot ” denotes the contraction of the second-order tensor with the vector $\nabla \rho$. The near-contact force \mathbf{F}_{rep} is discussed and modeled in Sec. 2.2.

Discrete derivatives. Whenever gradients/Laplacians of scalar fields (e.g. ρ , ϕ , μ_ϕ) are required in the forcing terms, we employ isotropic lattice-consistent stencils Shan (2006); Philippi *et al.* (2006); Thampi *et al.* (2013):

$$\nabla \Psi(\mathbf{x}) = \frac{1}{c_s^2} \sum_i w_i \Psi(\mathbf{x} + \mathbf{c}_i) \mathbf{c}_i, \quad (2.22)$$

$$\nabla^2 \Psi(\mathbf{x}) = \frac{1}{c_s^2} \left(\sum_{i \neq 0} w_i \Psi(\mathbf{x} + \mathbf{c}_i) - w_0 \Psi(\mathbf{x}) \right), \quad (2.23)$$

for a generic scalar field Ψ .

2.1.1. MUSCL scheme discretization for conservative Allen-Cahn equation

Conservative Allen–Cahn equation. The interface dynamics is captured through a phase field $\phi \in [0, 1]$, with $\phi = 1$ identifying the liquid phase and $\phi = 0$ the gas phase; the diffuse interface is conventionally located at $\phi_0 = 1/2$. Following our previous works Lauricella *et al.* (2025b), the evolution of ϕ is governed by the *conservative Allen–Cahn equation* (CACE) Chiu & Lin (2011):

$$\frac{\partial \phi}{\partial t} + \mathbf{u} \cdot \nabla \phi = D \nabla^2 \phi - \kappa \nabla \cdot (\phi(1 - \phi) \mathbf{n}), \quad (2.24)$$

where D is a (constant) interface diffusivity and \mathbf{n} is the interface normal,

$$\mathbf{n} = \frac{\nabla \phi}{|\nabla \phi|}. \quad (2.25)$$

The last term on the right-hand side of (2.24) is a compressive (anti-diffusive) flux that counteracts numerical diffusion and maintains a sharp, yet smooth, hyperbolic-tangent-like

interface profile across a prescribed thickness δ . A common choice, adopted here, links the compression strength to the diffusivity via

$$\kappa = \frac{4D}{\delta}, \quad (2.26)$$

so that the interface remains close to the target thickness throughout the simulation.

Conservative flux form. For the sake of numerical robustness, we cast the advective contribution in conservative form. Introducing the advective flux $\mathbf{F}_a = \mathbf{u}\phi$, Eq. (2.24) can be rewritten as

$$\frac{\partial \phi}{\partial t} + \nabla \cdot (\mathbf{u}\phi) = D \nabla^2 \phi - \kappa \nabla \cdot (\phi(1-\phi)\mathbf{n}), \quad (2.27)$$

so that mass conservation is enforced at the discrete level by a flux-difference update.

Discrete update in lattice units. In the implementation, the update at a fluid node (i, j, k) takes the form

$$\phi_{ijk}^{n+1} = \phi_{ijk}^n - (\nabla_h \cdot \mathbf{F}_a)_{ijk} + \tau_{\text{diff}} (\nabla_h^2 \phi)_{ijk} + S_{ijk}^{\text{comp}}, \quad (2.28)$$

where ∇_h denotes discrete operators on the Cartesian lattice, τ_{diff} collects the constants multiplying the discrete Laplacian (consistent with D in (2.24)), and S^{comp} represents the discrete counterpart of the compressive term $-\kappa \nabla \cdot (\phi(1-\phi)\mathbf{n})$. A double-buffering strategy is adopted, $\phi(\text{flip}) \rightarrow \phi(\text{flop})$, and the update is applied only to fluid nodes (solid nodes are skipped).

3D MUSCL–TVD (minmod) conservative advection for ϕ

Face fluxes and discrete divergence. Assuming $\Delta x = \Delta y = \Delta z = 1$, the discrete divergence of the advection flux is computed as

$$(\nabla_h \cdot \mathbf{F}_a)_{ijk} = \left(F_{i+\frac{1}{2},j,k}^x - F_{i-\frac{1}{2},j,k}^x \right) + \left(F_{i,j+\frac{1}{2},k}^y - F_{i,j-\frac{1}{2},k}^y \right) + \left(F_{i,j,k+\frac{1}{2}}^z - F_{i,j,k-\frac{1}{2}}^z \right), \quad (2.29)$$

with face fluxes

$$F_{i+\frac{1}{2},j,k}^x = u_{i+\frac{1}{2},j,k} \phi_{i+\frac{1}{2},j,k}^{\text{up}}, \quad F_{i,j+\frac{1}{2},k}^y = v_{i,j+\frac{1}{2},k} \phi_{i,j+\frac{1}{2},k}^{\text{up}}, \quad F_{i,j,k+\frac{1}{2}}^z = w_{i,j,k+\frac{1}{2}} \phi_{i,j,k+\frac{1}{2}}^{\text{up}}. \quad (2.30)$$

The face-centered velocities are obtained by arithmetic averages of cell-centered values, e.g. $u_{i+\frac{1}{2},j,k} = \frac{1}{2}(u_{i,j,k} + u_{i+1,j,k})$ (and similarly for v and w).

MUSCL reconstruction with minmod limiter. The upwind face value ϕ^{up} is computed with a MUSCL piecewise-linear reconstruction, limited by minmod to guarantee the TVD property. Along the x direction, the limited slope at cell (i, j, k) reads as:

$$s_{i,j,k}^x = \text{minmod}(\phi_{i,j,k} - \phi_{i-1,j,k}, \phi_{i+1,j,k} - \phi_{i,j,k}), \quad (2.31)$$

where

$$\text{minmod}(a, b) = \begin{cases} 0, & ab \leq 0, \\ \text{sign}(a) \min(|a|, |b|), & ab > 0. \end{cases} \quad (2.32)$$

The left/right reconstructed states at the face $i + \frac{1}{2}$ are then

$$\phi_{i+\frac{1}{2},j,k}^L = \phi_{i,j,k} + \frac{1}{2}s_{i,j,k}^x, \quad \phi_{i+\frac{1}{2},j,k}^R = \phi_{i+1,j,k} - \frac{1}{2}s_{i+1,j,k}^x, \quad (2.33)$$

and the upwind selection is

$$\phi_{i+\frac{1}{2},j,k}^{\text{up}} = \begin{cases} \phi_{i+\frac{1}{2},j,k}^L, & u_{i+\frac{1}{2},j,k} \geq 0, \\ \phi_{i+\frac{1}{2},j,k}^R, & u_{i+\frac{1}{2},j,k} < 0. \end{cases} \quad (2.34)$$

The same procedure is applied along y and z by replacing (i, u) with (j, v) and (k, w) , respectively. This scheme is second-order accurate in smooth regions, reverts to first order near sharp gradients, and prevents spurious oscillations at the interface.

Stencil requirements and boundary handling. The minmod slopes at $i \pm 1$ require accessing ϕ up to $i \pm 2$ (and analogously in y and z); hence, two buffer layers are required in each direction.

In periodic domains, buffer layers are filled by wrap-around; otherwise, they are filled consistently with the imposed boundary conditions.

Discrete compressive term and isotropic divergence

The compressive contribution in (2.24) can be interpreted as the divergence of a *compressive flux* $\mathbf{F}_c = \phi(1-\phi)\mathbf{n}$. In the code, its discrete divergence is evaluated with an isotropic D3Q27-based stencil, combining axis-, face-diagonal-, and body-diagonal contributions with weights (p_1, p_2, p_3) . Denoting by $\mathbf{a} = (a_x, a_y, a_z)$ the discrete representation of \mathbf{F}_c (or an equivalent compressive vector field), we compute

$$S_{ijk}^{\text{comp}} = -\frac{C_{\text{sharp}}}{c_s^2} (\nabla_h \cdot \mathbf{a})_{ijk}, \quad (2.35)$$

where C_{sharp} is the sharpening coefficient and c_s the lattice sound speed. The isotropic stencil reduces grid-orientation artifacts and yields a compressive contribution consistent with the discrete operators used by the LB solver.

2.2. Near-contact interaction model: theory and continuum formulation

2.2.1. Physical motivation: unresolved thin-film stabilization as a coarse-grained normal stress

In three-dimensional multiphase flows involving collisions and near-contact events (droplet impacts, dense emulsions, bubbly flows), the transition between coalescence and rebound is controlled by the dynamics of the thin intervening film that forms between two approaching interfaces Qian & Law (1997); Orme (1997). Coalescence requires this film to drain down to a critical thickness at which rupture is triggered by short-range intermolecular attraction (and/or by instability mechanisms), whereas rebound becomes possible if the film remains stable long enough for the interfaces to re-separate. Importantly, such a transition is not restricted to surfactant-laden systems: even in "clean" binary-fluid collisions, variations of fluid properties and droplet size can shift the outcome because they modify the characteristic drainage time and the attainable minimum film thickness.

Diffuse-interface simulations cannot directly resolve the nanometric scales associated with thin-film drainage and rupture Jacqmin (1999); Craster & Matar (2009). As a consequence, interfaces may merge prematurely for purely numerical reasons (insufficient resolution of the film, excessive overlap of diffuse interfaces, or missing unresolved repulsive physics), yielding spurious coalescence in regimes where physical systems would bounce Li (2016). To represent the stabilizing action of unresolved short-range interactions (steric/electrostatic/disjoining effects) and, more broadly, to *control* coalescence by delaying film collapse, at the mesoscopic level, we introduce a near-contact interaction (NCI) in the

form of an additional *purely normal* body force \mathbf{F}_{rep} . Such a force activates only when two diffuse interfaces approach each other with opposite orientations.

2.2.2. Interfacial indicator and geometric ingredients

We define the standard interfacial indicator

$$q(\phi) = \phi(1 - \phi) \in [0, 1/4], \quad (2.36)$$

which is maximal at $\phi = 1/2$ and vanishes in the bulk.

The key modeling requirement is to distinguish (i) an isolated interface (where q is nonzero but no thin film exists) from (ii) a true near-contact film configuration (where two interfaces face each other with opposite orientation). To this end, we introduce:

- an *activation function* $\chi_{\text{nc}}(\mathbf{x}) \in \{0, 1\}$ that identifies near-contact regions;
- a *partner mapping* $\mathbf{x}_p(\mathbf{x})$ that associates to an activated point \mathbf{x} a nearby point $\mathbf{y} = \mathbf{x}_p(\mathbf{x})$ located on the opposing interface across the film.

At the continuum level, χ_{nc} may be understood as indicating the existence, within a local neighborhood of \mathbf{x} , of a second interfacial location \mathbf{y} such that $q(\mathbf{y})$ is comparable to $q(\mathbf{x})$ and $\mathbf{n}(\mathbf{y})$ is sufficiently opposite to $\mathbf{n}(\mathbf{x})$. In practice, we realize this concept through a bounded local search on the lattice (no ray tracing); the discrete construction is reported later, but the theory below is expressed directly in terms of χ_{nc} and $\mathbf{x}_p(\mathbf{x})$.

2.2.3. Definition of the repulsive force: magnitude, facing factor, and antisymmetric normal direction

Let $\mathbf{y} = \mathbf{x}_p(\mathbf{x})$ be the partner point associated with \mathbf{x} when $\chi_{\text{nc}}(\mathbf{x}) = 1$. We define the paired interfacial indicator

$$q_1 = q(\phi(\mathbf{x})), \quad q_2 = q(\phi(\mathbf{y})), \quad q_{\text{pair}}(\mathbf{x}) = \frac{1}{2}(q_1 + q_2). \quad (2.37)$$

Using q_{pair} (rather than q_1 alone) improves symmetry across the film and reduces sensitivity to small discretization asymmetries.

Facing factor (activation strength). A scalar facing factor is introduced to modulate the interaction according to the degree of opposition of the two interfaces:

$$f_{\text{face}}(\mathbf{x}) = \max\left(0, -\mathbf{n}(\mathbf{x}) \cdot \mathbf{n}(\mathbf{y})\right) \in [0, 1]. \quad (2.38)$$

This factor is zero when normals are not opposing and approaches unity for nearly antiparallel normals.

Symmetric normal direction (antisymmetry and purely normal forcing). To ensure that the repulsion acts predominantly along the film-normal direction and exhibits an action–reaction structure, we define the symmetric direction

$$\mathbf{n}_{\text{sym}}(\mathbf{x}) = \frac{\mathbf{n}(\mathbf{x}) - \mathbf{n}(\mathbf{y})}{\|\mathbf{n}(\mathbf{x}) - \mathbf{n}(\mathbf{y})\|}, \quad (2.39)$$

with a fallback to the local line-of-centers direction when $\|\mathbf{n}(\mathbf{x}) - \mathbf{n}(\mathbf{y})\|$ is too small. Finally, we orient \mathbf{n}_{sym} consistently so that it points from \mathbf{x} toward the opposing interface (the partner cell), which guarantees that the partner experiences the opposite direction when the same construction is applied at \mathbf{y} . This choice (i) suppresses spurious tangential components and (ii) enhances antisymmetry of the interaction.

Repulsive flux and force density. We write the near-contact interaction as a repulsive “flux” \mathbf{J}_{rep} and the corresponding body-force density

$$\mathbf{F}_{\text{rep}}(\mathbf{x}) = \rho(\phi(\mathbf{x})) \mathbf{J}_{\text{rep}}(\mathbf{x}). \quad (2.40)$$

The closure adopted in this work is

$$\mathbf{J}_{\text{rep}}(\mathbf{x}) = A_{\text{rep}} \chi_{\text{nc}}(\mathbf{x}) q_{\text{pair}}(\mathbf{x}) w_h(h(q_{\text{pair}})) f_{\text{face}}(\mathbf{x}) \mathbf{n}_{\text{sym}}(\mathbf{x}). \quad (2.41)$$

Here A_{rep} is a tunable amplitude controlling the onset of non-coalescence, $h(q_{\text{pair}})$ is an analytical estimate of the film thickness derived in Sec. 2.2.4, and $w_h(h)$ is a bounded monotone weight that increases the repulsion as the film becomes thinner. A convenient and robust choice is

$$w_h(h) = \frac{1}{1 + (h/h_0)^p}, \quad h_0 = \mathcal{O}(\varepsilon), \quad p \geq 2, \quad (2.42)$$

while our reference implementation uses $p = 4$ and h_0 fixed in lattice units, i.e. $w_h(h) = 1/(1 + h^4)$.

Equation (2.41) makes explicit the intended separation of roles: q_{pair} localizes to the interface, f_{face} ensures that only opposing sheets interact, $w_h(h)$ concentrates the interaction in thin films, and \mathbf{n}_{sym} enforces a predominantly normal and antisymmetric response.

2.2.4. From phase-field overlap to an analytical film thickness

A central aspect of the present approach is that the film thickness is estimated *analytically* from the local phase-field indicator, with no need of ray tracing along the interface normal. The derivation exploits the equilibrium 1-D profile:

$$\phi(s) = \frac{1}{2} \left[1 + \tanh\left(\frac{2s}{\varepsilon}\right) \right], \quad (2.43)$$

Step 1: indicator profile along a planar interface. From $q(\phi) = \phi(1 - \phi)$ and (2.43), we obtain

$$q(s) = \frac{1}{4} \left[1 - \tanh^2\left(\frac{2s}{\varepsilon}\right) \right] = \frac{1}{4} \operatorname{sech}^2\left(\frac{2s}{\varepsilon}\right), \quad (2.44)$$

which is maximal at $s = 0$ and decays exponentially as $|s|/\varepsilon$ increases.

Step 2: inversion $q \mapsto s$. From (2.44),

$$\operatorname{sech}^2\left(\frac{2s}{\varepsilon}\right) = 4q, \quad \cosh\left(\frac{2s}{\varepsilon}\right) = \frac{1}{2\sqrt{q}},$$

hence

$$s(q) = \frac{\varepsilon}{2} \operatorname{arcosh}\left(\frac{1}{2\sqrt{q}}\right), \quad 0 < q \leq \frac{1}{4}. \quad (2.45)$$

Step 3: symmetric thin-film thickness. In a symmetric near-contact film formed by two opposing interfaces, the (half-)gap is approximated by s , and the film thickness is

$$h(q) \approx 2s(q) = \varepsilon \operatorname{arcosh}\left(\frac{1}{2\sqrt{q}}\right). \quad (2.46)$$

In our model we evaluate (2.46) using $q = q_{\text{pair}}$ from (2.37). We emphasize that (2.46) is intended to be used only within activated near-contact regions ($\chi_{\text{nc}} = 1$); outside such regions, q simply identifies an isolated diffuse interface and does not represent a physical film thickness.

Consistency and limitations. As $q \rightarrow 1/4^-$ (approaching an interface mid-surface), $h \rightarrow 0$ smoothly, while $h \rightarrow \infty$ as $q \rightarrow 0^+$ (bulk), in agreement with the interpretation of q as an overlap/thickness proxy in near-contact configurations.

2.2.5. Divergence-form (stress) representations and planar-limit disjoining pressure

For the sake of interpretability, it is worth expressing \mathbf{F}_{rep} as a divergence of a stress tensor, $\mathbf{F}_{\text{rep}} = \nabla \cdot \boldsymbol{\Sigma}_{\text{rep}}$ (at least approximately).

It is also interesting to note that for the equilibrium profile (2.43), one has

$$\frac{d\phi}{ds} = \frac{1}{\varepsilon} \operatorname{sech}^2\left(\frac{2s}{\varepsilon}\right), \quad (2.47)$$

and, using (2.44),

$$q(s) = \frac{1}{4} \operatorname{sech}^2\left(\frac{2s}{\varepsilon}\right) = \frac{\varepsilon}{4} \left| \frac{d\phi}{ds} \right|. \quad (2.48)$$

For a locally planar interface $\nabla\phi = (d\phi/ds) \mathbf{n}$, and therefore

$$q(\phi) \mathbf{n} = \frac{\varepsilon}{4} \nabla\phi. \quad (2.49)$$

This identity is exact for the 1-D equilibrium profile and provides a direct route to a repulsive pressure interpretation.

Exact isotropic pressure form in the locally planar, equilibrium limit. Assume locally planar equilibrium conditions and suppose that the thickness weight can be expressed as a function of ϕ along the profile, i.e. $w_h(h(q)) \equiv W(\phi)$ locally. Neglecting for the moment the facing modulation and activation (which take unit values in a perfectly symmetric film), the repulsive force (2.41) reduces to

$$\mathbf{F}_{\text{rep}} = \rho A_{\text{rep}} q(\phi) W(\phi) \mathbf{n}. \quad (2.50)$$

Using (2.49),

$$\mathbf{F}_{\text{rep}} = \rho A_{\text{rep}} \frac{\varepsilon}{4} W(\phi) \nabla\phi = \nabla\Pi(\phi), \quad (2.51)$$

where the scalar potential $\Pi(\phi)$ is

$$\mathbf{F}_{\text{rep}} = \nabla \cdot (\Pi(\phi) \mathbf{I}), \quad \Pi(\phi) = A_{\text{rep}} \frac{\varepsilon}{4} \int^{\phi} \rho(\xi) W(\xi) d\xi. \quad (2.52)$$

Thus, in the locally planar equilibrium limit, the near-contact repulsion is exactly equivalent to the gradient of an isotropic, positive "disjoining pressure" $\Pi(\phi)$.

General normal-stress form away from the planar limit. Away from the planar limit (curvature, non-equilibrium, spatial variability), a natural stress representation is a predominantly normal interfacial stress

$$\mathbf{F}_{\text{rep}} = \nabla \cdot (\Pi_{\text{nc}} \mathbf{n}_{\text{sym}} \otimes \mathbf{n}_{\text{sym}}), \quad (2.53)$$

where $\Pi_{\text{nc}}(\mathbf{x})$ is an effective near-contact normal stress amplitude. Decomposing (2.53) along the normal coordinate s associated with \mathbf{n}_{sym} and denoting by $\kappa = \nabla \cdot \mathbf{n}_{\text{sym}}$ the mean curvature of the normal field, one obtains (formally)

$$\nabla \cdot (\Pi_{\text{nc}} \mathbf{n}_{\text{sym}} \otimes \mathbf{n}_{\text{sym}}) = (\partial_s \Pi_{\text{nc}} + \kappa \Pi_{\text{nc}}) \mathbf{n}_{\text{sym}} + \Pi_{\text{nc}} (\mathbf{n}_{\text{sym}} \cdot \nabla) \mathbf{n}_{\text{sym}, \perp}, \quad (2.54)$$

where the second term is tangential and vanishes for planar configurations (and is $O(\kappa)$ for gentle curvature). Matching the leading normal component of (2.54) to the model forcing direction in (2.41) yields a normal-balance relation for Π_{nc} :

$$\partial_s \Pi_{\text{nc}} + \kappa \Pi_{\text{nc}} \approx \rho A_{\text{rep}} \chi_{\text{nc}} q_{\text{pair}} w_h(h(q_{\text{pair}})) f_{\text{face}}. \quad (2.55)$$

In the locally planar case ($\kappa \simeq 0$), (2.55) reduces to $\partial_s \Pi_{\text{nc}} \approx (\dots)$ and the isotropic disjoining-pressure picture (2.52) is recovered when the dependence can be expressed through ϕ along an equilibrium profile.

The construction (2.41) is designed to be mainly normal through \mathbf{n}_{sym} . If a strictly tangential-free representation is desired at the discrete level, one may also consider adding an isotropic counter-stress on the tangent plane. In practice, we find that the symmetric-normal choice already suppresses spurious tangential contributions and provides robust near-contact stabilization.

2.2.6. Summary of the closure and model parameters

Collecting the definitions, the near-contact interaction entering in (2.2) is

$$\mathbf{F}_{\text{rep}}(\mathbf{x}) = \rho(\phi(\mathbf{x})) A_{\text{rep}} \chi_{\text{nc}}(\mathbf{x}) q_{\text{pair}}(\mathbf{x}) w_h(h(q_{\text{pair}})) f_{\text{face}}(\mathbf{x}) \mathbf{n}_{\text{sym}}(\mathbf{x}), \quad (2.56)$$

with q_{pair} from (2.37), f_{face} from (2.38), \mathbf{n}_{sym} from (2.39), and $h(q)$ from (2.46).

The free parameters are: (i) A_{rep} , controlling the onset of non-coalescence and the overall strength of the near-contact barrier; (ii) the thickness-weight parameters (h_0, p) in (2.42), setting how sharply repulsion concentrates as films thin; (iii) the activation/pairing thresholds implicitly contained in χ_{nc} (interfacial gate, facing threshold, neighborhood radius). Their discrete construction is reported in the Numerical Methods section; importantly, the method avoids ray tracing along interface normals and relies instead on a bounded local detection combined with the analytical mapping (2.46).

2.3. Numerical implementation of the near-contact interaction

This section describes how the near-contact interaction (NCI) is evaluated on the lattice in a manner that is (i) strictly local, (ii) efficient on GPUs, and (iii) robust in enforcing a *facing-interface* activation (thin-film configurations only), without ray tracing or normal-line marching. The implementation is organized into two steps executed at each time step: (1) *thin-film detection and pairing*, which builds an activation mask and a partner map, and (2) *flux/force construction*, which uses the analytical film-thickness estimate and returns a purely normal, antisymmetric repulsive forcing.

2.3.1. Discrete geometric fields and interfacial gate

We assume that the phase field ϕ is available at cell centers. We first compute the interface normal field

$$\mathbf{n}(\mathbf{x}) = \frac{\nabla\phi(\mathbf{x})}{\|\nabla\phi(\mathbf{x})\| + \epsilon_n}, \quad (2.57)$$

where ϵ_n is a small regularization parameter. In practice, $\nabla\phi$ is evaluated with an isotropic stencil consistent with the lattice (e.g. D3Q27 isotropic gradient) to minimize directional bias.

We also compute the interfacial indicator

$$q(\mathbf{x}) = \phi(\mathbf{x})(1 - \phi(\mathbf{x})), \quad (2.58)$$

with ϕ clamped to $[0, 1]$ when needed (as in the code) to avoid small overshoots affecting the gate. A cell is considered *interfacial* if

$$q(\mathbf{x}) \geq q_{\text{th}}, \quad (2.59)$$

where q_{th} is a small threshold (typically $q_{\text{th}} \ll 1/4$). This gate restricts the search to cells located within the diffuse interfacial band.

2.3.2. Thin-film detection and partner selection

Overview. The purpose of detection is to activate the NCI "on-demand". i.e. only in regions where two interfaces are in near contact *and* face each other. At each cell \mathbf{x} satisfying (2.59),

we search in a bounded cubic neighborhood (window radius w):

$$\mathcal{W}(\mathbf{x}) = \{\mathbf{x} + \mathbf{r} : \mathbf{r} = (d_i, d_j, d_k), d_\alpha \in [-w, w], \mathbf{r} \neq \mathbf{0}\}, \quad (2.60)$$

and attempt to identify a *partner* cell $\mathbf{y} \in \mathcal{W}(\mathbf{x})$ located on the opposing interface across the film.

We store: (i) a binary activation mask $\chi_{\text{nc}}(\mathbf{x}) \in \{0, 1\}$, and (ii) an integer partner map $\mathbf{x}_p(\mathbf{x})$.

Candidate acceptance criteria. A neighbor cell $\mathbf{y} \in \mathcal{W}(\mathbf{x})$ qualifies as a valid partner candidate if it satisfies three conditions:

(i) **Interfacial neighbor gate:** $q(\mathbf{y}) \geq q_{\text{th}}$.

(ii) **Iso-interface similarity:**

$$|q(\mathbf{y}) - q(\mathbf{x})| \leq \eta \max(q(\mathbf{x}), \epsilon_q), \quad (2.61)$$

with $\eta = 0.1$ in our implementation and ϵ_q a small floor. This enforces that the two points lie at comparable locations within the diffuse interface (e.g. both close to $\phi \simeq 1/2$), which improves symmetry and reduces false positives where an interfacial cell pairs with a near-bulk cell.

(iii) **Facing condition (opposing normals):**

$$\mathbf{n}(\mathbf{x}) \cdot \mathbf{n}(\mathbf{y}) \leq \cos \theta_{\text{opp}}, \quad (2.62)$$

where θ_{opp} is an ‘‘opposition’’ angle (e.g. close to π). This prevents activation on the same interface sheet.

In addition, for each accepted candidate, we define a *facing score* used both for tie-breaking and later for the force magnitude. Consistent with the forcing stage, we use

$$f_{\text{face}}(\mathbf{x}, \mathbf{y}) = \max(0, -\mathbf{n}(\mathbf{x}) \cdot \mathbf{n}(\mathbf{y})) \in [0, 1]. \quad (2.63)$$

(Any equivalent monotone mapping of the dot product can be used; our code, *accLB*, uses an affine mapping for selection and (2.63) for the final forcing, which are consistent up to monotone rescaling.)

Nearest-partner selection rule. Among all accepted candidates, we choose the partner \mathbf{y}_{best} as the *nearest* one in Euclidean distance,

$$\mathbf{y}_{\text{best}} = \arg \min_{\mathbf{y} \in C(\mathbf{x})} |\mathbf{y} - \mathbf{x}|^2, \quad (2.64)$$

where $C(\mathbf{x})$ is the set of accepted candidates. If multiple candidates share the same minimal distance (ties), we choose the one with the largest facing score $f_{\text{face}}(\mathbf{x}, \mathbf{y})$. Finally,

$$\chi_{\text{nc}}(\mathbf{x}) = \begin{cases} 1, & \text{if at least one candidate exists,} \\ 0, & \text{otherwise,} \end{cases} \quad \mathbf{x}_p(\mathbf{x}) = \begin{cases} \mathbf{y}_{\text{best}}, & \chi_{\text{nc}}(\mathbf{x}) = 1, \\ \mathbf{0}, & \chi_{\text{nc}}(\mathbf{x}) = 0. \end{cases} \quad (2.65)$$

Remarks on locality and robustness.

- The method is *fully local* (bounded window) and thus GPU-friendly: the detection cost scales as $O(N(2w + 1)^3)$ with a small, fixed w .

- The facing criterion (2.62) is the key ingredient that distinguishes a true thin-film configuration (two opposing sheets) from a single interface (for which nearby interfacial points exist but have similar normals).

- The similarity gate (2.61) improves antisymmetry and consistency of the subsequent analytical thickness estimate, because it tends to pair points at comparable ‘‘depth’’ inside the diffuse interface.

2.3.3. Repulsive forcing construction from the partner map

Once χ_{nc} and \mathbf{x}_p are available, we compute a purely normal repulsive forcing at each activated cell.

Paired indicator and clamping Let $\mathbf{y} = \mathbf{x}_p(\mathbf{x})$ for an activated \mathbf{x} . We define

$$q_1 = q(\mathbf{x}), \quad q_2 = q(\mathbf{y}), \quad q_{\text{pair}} = \frac{1}{2}(q_1 + q_2). \quad (2.66)$$

To avoid numerical issues in the film-thickness mapping (which involves \sqrt{q} and arcosh), we clamp

$$q_{\text{cl}} = \min(\max(q_{\text{pair}}, \epsilon_q), 1/4 - \epsilon_q), \quad (2.67)$$

with ϵ_q a small number.

Facing factor and symmetric normal direction We compute the facing factor (same as in the theory section)

$$f_{\text{face}} = \max(0, -\mathbf{n}(\mathbf{x}) \cdot \mathbf{n}(\mathbf{y})). \quad (2.68)$$

If f_{face} is zero, the interaction is suppressed.

We then build the symmetric normal direction

$$\tilde{\mathbf{n}}_{\text{sym}} = \mathbf{n}(\mathbf{x}) - \mathbf{n}(\mathbf{y}), \quad \mathbf{n}_{\text{sym}} = \frac{\tilde{\mathbf{n}}_{\text{sym}}}{\|\tilde{\mathbf{n}}_{\text{sym}}\| + \epsilon_n}, \quad (2.69)$$

with fallback to the line-of-centers unit vector

$$\hat{\mathbf{r}} = \frac{\mathbf{y} - \mathbf{x}}{\|\mathbf{y} - \mathbf{x}\|}$$

when $\|\tilde{\mathbf{n}}_{\text{sym}}\|$ is too small. Finally, we orient \mathbf{n}_{sym} so that $\hat{\mathbf{r}} \cdot \mathbf{n}_{\text{sym}} \geq 0$. This convention ensures that the partner cell, when processed, produces the opposite direction, enhancing action–reaction behavior.

Analytical film thickness and thickness weight A key advantage of the present approach is that the film thickness is estimated *analytically* from q_{cl} . Using the equilibrium profile derived in Sec. 2.2.4, we compute

$$h = \varepsilon \text{arcosh}\left(\frac{1}{2\sqrt{q_{\text{cl}}}}\right), \quad (2.70)$$

where ε is the diffuse-interface thickness scale. We then evaluate the bounded thickness weight $w_h(h)$; the reference implementation uses

$$w_h(h) = \frac{1}{1 + h^4}, \quad (2.71)$$

which is a particular case of the general form $w_h(h) = 1/(1 + (h/h_0)^p)$ with $p = 4$ and $h_0 = 1$ in lattice units. This choice makes the repulsion effectively switch on only when $h = \mathcal{O}(1)$ in lattice units (i.e. when the diffuse interfaces are genuinely close), while remaining bounded.

Final repulsive flux and force With these ingredients, the discrete repulsive flux is

$$\mathbf{J}_{\text{rep}}(\mathbf{x}) = A_{\text{rep}} \chi_{\text{nc}}(\mathbf{x}) q_{\text{cl}}(\mathbf{x}) w_h(h) f_{\text{face}}(\mathbf{x}) \mathbf{n}_{\text{sym}}(\mathbf{x}), \quad (2.72)$$

and the force density entering the momentum equation is

$$\mathbf{F}_{\text{rep}}(\mathbf{x}) = \rho(\phi(\mathbf{x})) \mathbf{J}_{\text{rep}}(\mathbf{x}). \quad (2.73)$$

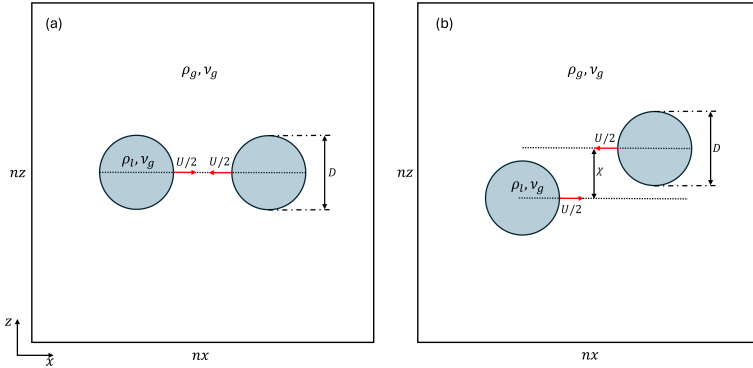


Figure 1: Graphical sketch of the head-on (a) and off-axis (b) collisions between equally sized droplets.

3. Results

3.1. Head-on and off axis impacts between non-coalescing droplets: comparison with experiments

To validate the proposed near-contact interaction (NCI) in a regime where the collision outcome is controlled by the unresolved thin gas film, we reproduce two reference experiments from Huang & Pan Huang & Pan (2021) featuring clean droplet bouncing at comparable Weber numbers but different droplet sizes and impact parameters. Specifically, we consider (i) a head-on collision of dodecane droplets with diameter $D = 300 \mu\text{m}$ at $We = 4.60$ and $B = 0$, and (ii) an off-axis collision of water droplets with diameter $D = 1000 \mu\text{m}$ at $We = 4.77$ and $B = 0.32$ Huang & Pan (2021) (see figure 1 for a graphical sketch of the experimental setup). Here, the Weber number is defined as $We = \rho_\ell U^2 D / \sigma$, and the impact parameter as $B = \chi / D$, with χ the offset between droplet centres measured in the direction normal to the relative velocity (collision plane) Huang & Pan (2021). These two cases (reported in Fig. 2) are particularly stringent benchmarks for diffuse-interface models because the physically relevant film thickness at rebound remains far below the computational interfacial thickness; without an additional short-range stabilization mechanism, premature interface overlap typically leads to spurious coalescence. All simulations are performed in a fully periodic cubic domain of size 512^3 lattice units (lu). Each droplet has diameter $D_{lu} = 80$, which sets the spatial mapping $\Delta x = D / D_{lu}$; this yields $\Delta x = 3.75 \mu\text{m}$ for the $D = 300 \mu\text{m}$ head-on case and $\Delta x = 12.5 \mu\text{m}$ for the $D = 1000 \mu\text{m}$ off-axis case. The density ratio is fixed to $\rho_\ell / \rho_g = 1000$, and the surface tension is set to $\sigma = 0.02$ (lu). Kinematic viscosities are prescribed in lattice units and selected so that the simulations match the experimental nondimensional conditions (in particular We , and the associated inertio-capillary time scale): for the head-on case we use $\nu_\ell = 0.005$ and $\nu_g = 0.05$ (lu), whereas for the off-axis case $\nu_\ell = 0.0012$ and $\nu_g = 0.012$ (lu). In all comparisons, the reported time is expressed in milliseconds, consistently with the experimental sequences Huang & Pan (2021).

Figure 2 provides a direct visual comparison between the experimental silhouettes (top rows) and the numerical interfaces (bottom rows). In the head-on collision at $D = 300 \mu\text{m}$ and $We = 4.60$, the simulation reproduces the symmetric approach, the progressive flattening at impact, and the subsequent rebound without coalescence, with a close match of the deformation levels and of the rebound timing (the droplets detach at $t \simeq 0.85\text{--}0.90$ ms in both experiment and simulation). In the off-axis case ($D = 1000 \mu\text{m}$, $We = 4.77$, $B = 0.32$), the model captures the oblique interaction sequence: the droplets undergo asymmetric deformation, exchange tangential momentum during near-contact, and then re-separate while

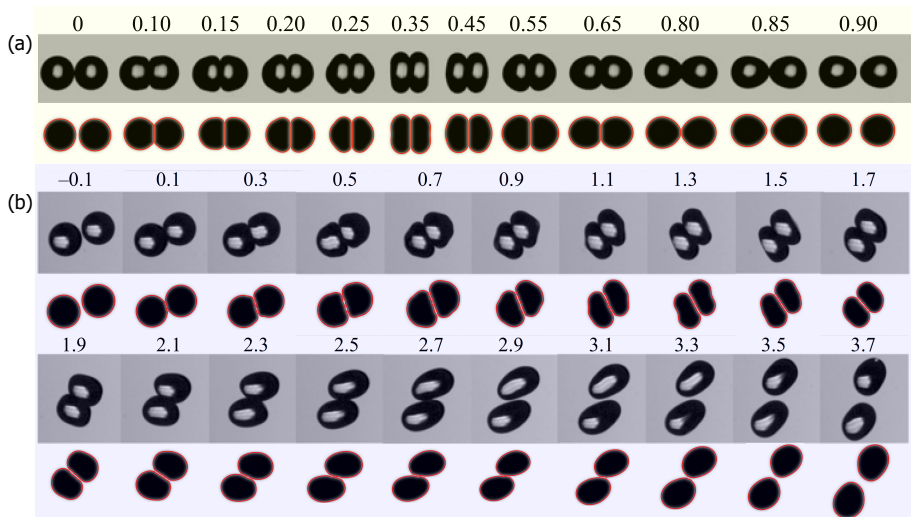


Figure 2: Comparison between experimental results of Huang & Pan Huang & Pan (2021) and the corresponding numerical simulations for two bouncing regimes. (a) Head-on collision of dodecane droplets with $D = 300 \mu\text{m}$ at $We = 4.60$. (b) Off-center collision of water droplets with $D = 1000 \mu\text{m}$, $B = 0.32$ and $We = 4.70$. In each case, experiments (top) and simulations (bottom) are shown for direct comparison. The time shown above each frame is given in milliseconds.

preserving distinct interfaces, reproducing the experimentally observed post-impact shapes and the qualitative trajectory/rotation pattern over the full temporal window up to $t = 3.7$ ms. Minor discrepancies at late times are expected because the experimental images are 2D projections of a 3D event and because small differences in the initial alignment/relative phase can affect the long-time drift after rebound; nonetheless, the agreement across both a head-on and an off-center configuration indicates that the NCI provides the missing short-range stabilization required to recover the correct non-coalescing outcome within a diffuse-interface framework.

3.2. Thin-film hydrodynamics during droplets impact

Flow-field signatures of thin-film sustenance and rebound (head-on case). To further substantiate that the proposed NCI reproduces not only the interface kinematics but also the *mechanism* responsible for non-coalescence, Fig. 3 reports a sequence of velocity fields during the head-on impact (colormap: normalized velocity magnitude u/u_{max} ; arrows: unit vectors, i.e. direction only). At early times (panel a), the flow in the inter-droplet film is intense and predominantly directed *outwards* along the collision plane, consistent with a lubrication-type squeezing/draining flow driven by the rapid reduction of the gap. At the same stage, the velocity within each droplet remains almost undisturbed: the core motion is essentially uniform and aligned with the impact direction (x -axis), indicating that the internal flow has not yet strongly reorganized in response to the impending near-contact interaction. As the droplets reach the closest approach (panels b–c), the velocity within the thin film *drops sharply* (blue region in the colormap) and the in-plane flow direction in the film *inverts*, highlighting the onset of a sustained interfacial separation. In parallel, the internal droplet flow departs from the initial plug-like motion: the rear side of each droplet still moves towards the impact region, whereas near the front (close to the interaction zone) the flow becomes predominantly tangential to the interface. This reorientation is a clear signature of

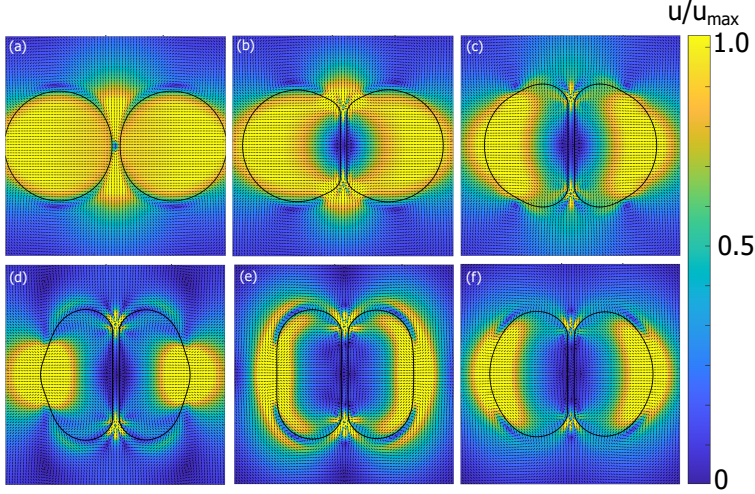


Figure 3: Velocity field in the inter-droplet region during head-on impact. The color map denotes the normalized velocity magnitude (u/u_{\max}), and arrows indicate the flow direction.

the pressure build-up in the film and of the associated redistribution of momentum within the droplets, which is a necessary condition for rebound without coalescence. A distinctive feature is observed at the *rim* (tip) of the thin film (panels c–d): the velocity vectors display a localized recirculation pattern, i.e. the flow is diverted and turns back rather than feeding through the film.

This is consistent with the fact that, during the interaction, the film behaves as a highly resistive lubrication layer: the outward draining is progressively impeded, the fluid is redirected around the film edge, and the resulting recirculation contributes to maintaining a finite separation up to the rebound stage. In the later stages (panels e - f), the velocity within the film remains comparatively small, whereas the flow inside the droplets *reverses* and becomes directed outward with respect to the collision direction, consistent with the global bouncing motion and the relaxation of the deformed interfaces after the closest approach.

To keep the above discussion quantitative, we report two local diagnostics extracted from the numerical fields. First, Fig. 4 shows the film-averaged normal velocity $\bar{w}_{\text{film}}(z)$, obtained by averaging w across the instantaneous interfacial gap (identified between the two facing $\rho = \rho_{\text{iso}}$ iso-contours) at each z . In the pre-impact stage, \bar{w}_{film} exhibits opposite signs on the two sides of the film centerline z_0 : it is negative for $z > z_0$ and positive for $z < z_0$, consistently with a strong drainage pattern where the film flow is directed away from the interaction region with opposite orientation in the two semi-domains. As the droplets approach their minimum separation, the magnitude of \bar{w}_{film} collapses towards zero over most of the interaction region, indicating that the through-film flux is strongly reduced when the lubrication resistance becomes dominant. At later times, \bar{w}_{film} remains small and displays a reversal of the sign distribution compared with the early stage, providing a compact quantitative signature of the flow inversion in the thin film discussed above. Second, Fig. 4 reports the centerline profiles of the streamwise velocity $u_x(x)$ extracted along a fixed line $z = z_0$ inside the impacting droplet. In the pre-impact stage (panel (a)), u_x is nearly constant throughout most of the droplet extent along x , indicating an almost plug-like internal motion aligned with the collision direction. During the interaction (panel (b)), the profile departs from this uniform state and progressively decreases towards the front region facing the thin film, approaching vanishing values in the vicinity of the interface. In the post-impact stage (panel (c)), this

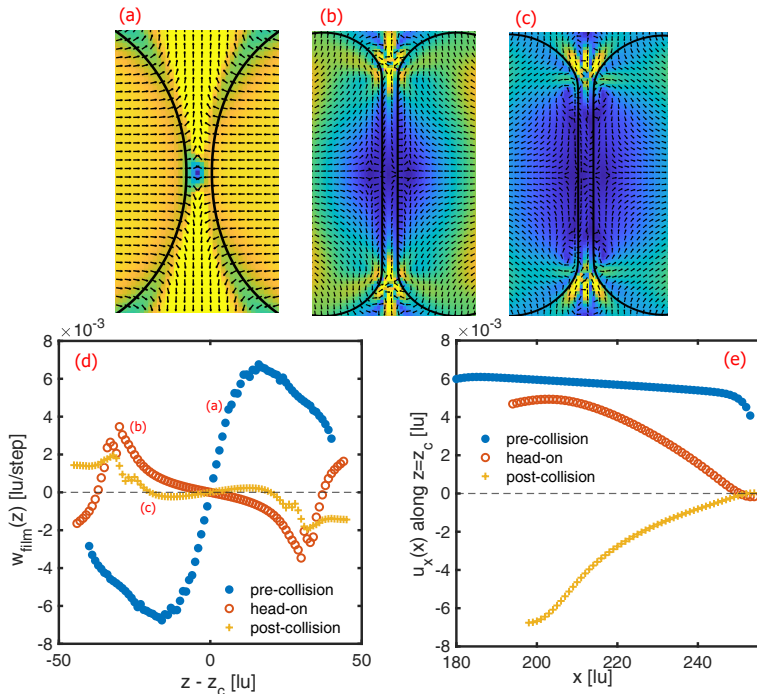


Figure 4: Velocity field and associated profiles at three stages of the collision. Panels (a–c) show the flow field at the pre-collision stage, at head-on contact, and the post-collision. Panel (d) reports the film-averaged normal velocity \bar{w}_{film} , and panel (e) shows the centerline streamwise velocity $u_x(x)$ along $z = z_0$. In panels (d) and (e), the blue, orange, and yellow curves correspond to the stages shown in panels (a–c), respectively.

front-region attenuation persists and extends over a wider portion of the droplet, consistent with the emergence of a stagnation-like zone induced by the strong hydrodynamic resistance of the film and with a redistribution of momentum away from the incoming streamwise component. Together, these two diagnostics support the mechanistic picture inferred from the vector fields: the film drainage initially dominates, then the film flux is suppressed and reverses while the incoming axial motion is locally arrested near the impact region, enabling thin-film sustenance and subsequent rebound without coalescence.

3.3. Self-tuning of the repulsive near contact force

In this section, we report on an apparently counterintuitive feature observed when varying the near-contact repulsive amplitude A_{rep} : once A_{rep} exceeds the threshold required to prevent coalescence, further increases of A_{rep} produce no discernible change in the macroscopic impact dynamics (e.g. rebound/approach kinematics, deformation patterns, and the overall evolution of the colliding droplets). In other words, the collision outcome and the gross flow features appear remarkably insensitive to the nominal strength of the repulsive model, provided that the system operates in the non-coalescing regime. This observation suggests that the near-contact interaction does not act as a simple linear penalty factor (for which one would expect a monotonic increase of repulsive stresses and a strong sensitivity of the dynamics to A_{rep}), but rather as an *adaptive barrier* that delivers the level of normal resistance required by the local thin-film force balance. To test this hypothesis and rationalize the observed macroscopic robustness, we quantify the near-contact and capillary actions inside the film by constructing a set of key observables computed at the instant of maximum activation (i.e. the

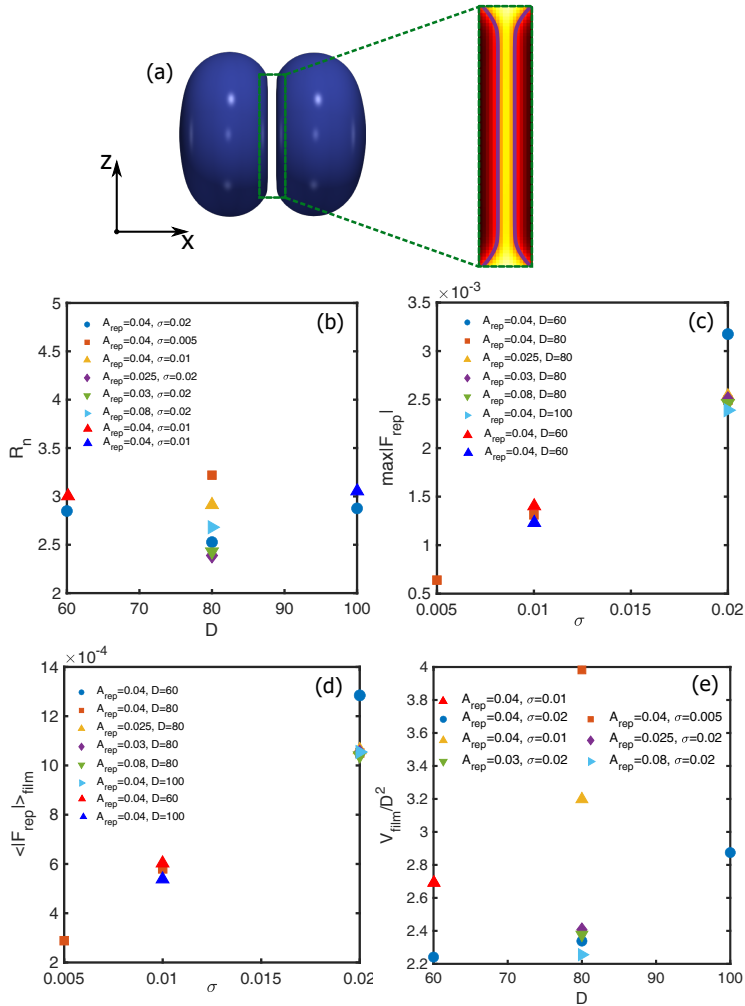


Figure 5: Quantification of the near-contact interaction and the capillary contribution within the inter-droplet film at peak activation for different values of A_{rep} , σ , and D . (a) Schematic of the inter-droplet thin-film region where the force balance is evaluated. (b) Ratio between the repulsive and capillary forces within the thin film, R_n , as a function of droplet diameter. (c) Maximum repulsive force magnitude $\max |F_{rep}|$ as a function of σ . (d) Film-averaged repulsive force magnitude $\langle |F_{rep}| \rangle_{film}$ as a function of σ . (e) Activated film volume normalized by the square of the droplet diameter V_{film}/D^2 as a function of D .

time at which the near-contact region is maximally activated). Specifically, we (i) compare the repulsive and capillary force components projected along the local interface normal, (ii) monitor the absolute intensity of the repulsive forcing (peak and mean), and (iii) characterize how the extent of the interaction region varies with droplet diameter D , surface tension σ , and model amplitude A_{rep} . The resulting trends are summarized in Fig. 5.

Figure 5(a) reports the ratio

$$R_n \equiv \frac{\int_{\Omega_{\text{film}}} |\mathbf{F}_{\text{rep}} \cdot \mathbf{n}| dV}{\int_{\Omega_{\text{film}}} |\mathbf{F}_{\text{cap}} \cdot \mathbf{n}| dV}, \quad (3.1)$$

where Ω_{film} denotes the near-contact (thin-film) region identified by activation of the repulsive model, \mathbf{n} is the local unit normal to the interface (computed from the phase-field gradient), \mathbf{F}_{rep} is the repulsive force density (per unit volume) produced by the near-contact interaction, and \mathbf{F}_{cap} is the capillary force density. Symbols distinguish the values of A_{rep} , while the color encodes σ . The central result is that R_n remains of the same order across the explored parameter space and is only weakly dependent on D , A_{rep} , and σ (in particular is only weakly dependent on their ratio). This shows that the repulsive action in the film remains consistently commensurate with the capillary action: the near-contact interaction does not "over-enforce" separation when A_{rep} is increased, but instead supplies a normal resistance whose magnitude remains comparable to the capillary-driven normal forcing that promotes interface approach. This is the quantitative signature of a self-tuned near-contact barrier, and it explains why the overall impact dynamics is largely insensitive to changes in A_{rep} once the non-coalescing regime is reached.

While Fig. 5(a) addresses the relative balance between repulsion and capillarity, Figs. 5(b)–(c) clarify how the absolute level of the repulsive forcing varies when physical parameters are modified. In particular, Fig. 5(b) shows the peak repulsive intensity $\max |\mathbf{F}_{\text{rep}}|$ and Fig. 5(c) reports the film-averaged magnitude $\langle |\mathbf{F}_{\text{rep}}| \rangle_{\text{film}}$ (computed as the integral of $|\mathbf{F}_{\text{rep}}|$ over Ω_{film} divided by the activated film volume). When σ is decreased, both the peak and the average repulsive levels decrease accordingly. This is consistent with an adaptive mechanism in which the repulsive forcing scale tracks the capillary scale: lowering σ reduces the capillary forcing level and the near-contact interaction correspondingly relaxes in absolute amplitude, without requiring a retuning of A_{rep} to preserve a comparable repulsion–capillarity balance. At the same time, changes in droplet size mainly affect the geometry of the interaction (how large the active film region becomes) rather than substantially altering the characteristic repulsive forcing level inside the film, supporting again the interpretation of a regulated barrier.

Finally, Fig. 5(d) reports the activated film volume V_{film} divided by D^2 . This quantity provides a compact measure of the extent of the near-contact region, disentangling the trivial size effect (area-like scaling $\sim D^2$) from changes in activation thickness/patchiness. The weak dependence of V_{film}/D^2 on D indicates that the near-contact region scales primarily with droplet size, while variations of σ and A_{rep} modulate the degree of activation of the film. Importantly, the combined view of panels (a) and (d) indicates that the near-contact interaction stabilizes the collision mostly by adjusting the support of the repulsive action (how many cells participate in Ω_{film} at peak activation) rather than by generating disproportionately large local extremes. This "support-adjustment" mechanism provides a natural explanation for the observed robustness: the near-contact model self-organizes a thin-film repulsive forcing comparable to the capillary forcing, thereby maintaining a stable, non-coalescing film over a wide range of parameters.

In passing we note that, below a critical A_{rep} , the above self-tuning can no longer be maintained: the activated film region becomes intermittent and collapses, and a topology change (coalescence) may occur even if local repulsive peaks are present. This highlights that stability requires not only a sufficiently strong local repulsion but also a sufficiently extended and persistent near-contact region at maximum activation.

3.4. Multi-body interactions: rising bubble swarm in a quiescent environment

A central objective of the present near-contact interaction (NCI) framework is to enable *robust many-body interface dynamics* within a diffuse-interface formulation, i.e. configurations in which a large number of deformable bubbles undergo repeated close approaches, collisions, and collective rearrangements without triggering spurious topology changes. In this subsection we therefore demonstrate the capability of the present model to stably handle dense multi-bubble interactions in three dimensions over long integration times.

To this aim, we consider a swarm of bubbles rising in an otherwise quiescent carrier liquid within a fully periodic cubic domain of size $N_x \times N_y \times N_z = 512^3$ (lattice units). The surface tension is set to $\sigma = 0.01$ (lu), the liquid and gas kinematic viscosities are $\nu_\ell = 10^{-3}$ and $\nu_g = 10^{-2}$ (lu), respectively, and the density ratio is fixed to $\rho_\ell/\rho_g = 1000$. Buoyancy is modeled through a constant body acceleration $g = 10^{-5}$ (lu/step), applied in the vertical direction. The initial condition consists of $N_b = 100$ spherical bubbles, corresponding to an overall gas volume occupation of approximately 8%.

For this configuration, the dynamical regime can be characterized in terms of dimensionless groups defined using a characteristic bubble diameter D and a characteristic rise velocity U_b (e.g. obtained from the mean bubble centroid velocity). In particular, we introduce the bubble Reynolds and Weber numbers

$$Re_b = \frac{U_b D}{\nu_\ell}, \quad We_b = \frac{\rho_\ell U_b^2 D}{\sigma}, \quad (3.2)$$

together with the Galilei number

$$Ga = \frac{\sqrt{g D^3}}{\nu_\ell}. \quad (3.3)$$

In the present simulations, these quantities evaluate to

$$Re_b = 1500, \quad We_b = 37.5, \quad Ga = 1500, \quad (3.4)$$

and will be reported based on the measured U_b and the initial bubble diameter D .

Figure 6 provides a qualitative and quantitative overview of the multi-body dynamics. Panels (a)–(f) show six representative snapshots of the bubble field at increasing times. Despite the high number of interfaces and the frequent near-contact events occurring during the collective rise and rearrangement, the bubble population remains well separated this highlighting the effective frustration of coalescence imposed by the short range repulsion. This is a stringent test for phase-field approaches, as dense swarms can easily develop numerical coalescence when the interfacial transport is not sufficiently robust or when close-range interactions are not properly regularized. The present results indicate that the present LB-Allen-Cahn model augmented with NCI provides stable and scalable handling of many-body interactions in a fully periodic 512^3 domain. To quantify the preservation of the dispersed phase, Fig.6 also reports the probability density functions (PDFs) of the interfacial mean curvature κ and of the bubble equivalent diameter D_{eq} (computed from the instantaneous bubble volumes). The curvature distribution exhibits a clear peak associated with the initialization radius $R \simeq 30$ (lu), consistently with the spherical relation for the mean curvature,

$$\kappa = \nabla \cdot \mathbf{n} = \frac{2}{R} \quad \Rightarrow \quad R = \frac{2}{\kappa}, \quad (3.5)$$

where \mathbf{n} is the outward unit normal to the interface. Coherently, the diameter PDF is sharply peaked around $D_{\text{eq}} \simeq 2R$, highlighting a quasi-monodisperse population and indicating that, over the time window considered, multi-body interactions predominantly lead to rear-

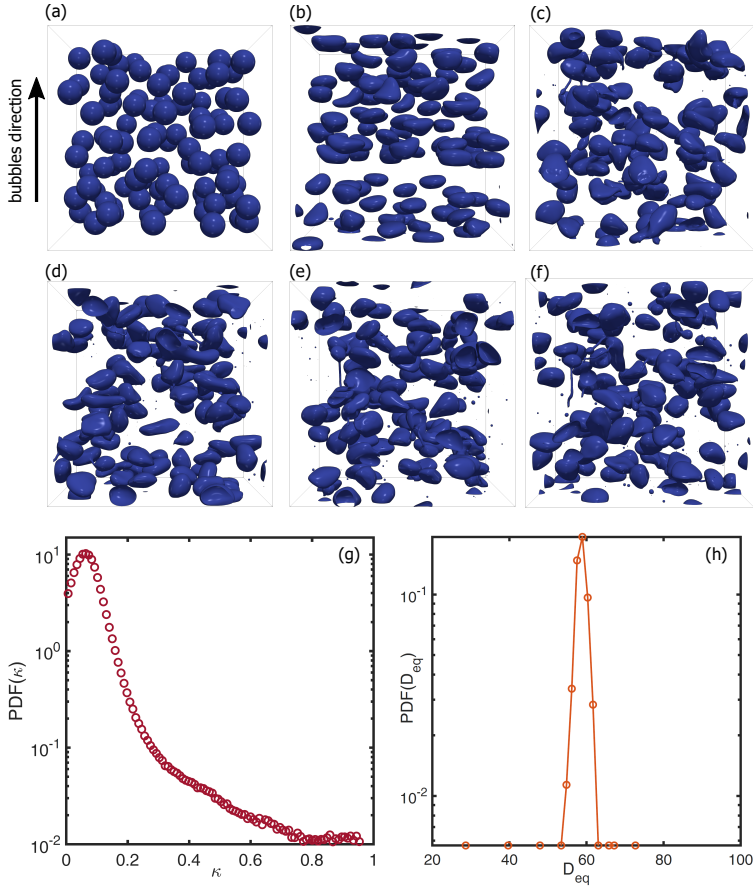


Figure 6: Evolution of a swarm of bubbles rising in a periodic cubic domain. The simulation corresponds to $Re_b = 1500$, $We_b = 37.5$, and $Ga = 1500$. (a–f) Snapshots of the bubble configuration at increasing times. (g) PDF of the surface curvature. (h) PDF of the equivalent diameter.

rangements and transient deformations rather than coalescence-driven growth. Overall, these statistics confirm that the proposed framework can sustain dense three-dimensional bubble swarms while preserving bubble identity and delivering stable curvature/size distributions suitable for subsequent analyses of dispersity, clustering, and interface-mediated transfer mechanisms. Complementing the interface-only visualization in Fig. 6, Fig. 7 reports eight snapshots (panels a–h) of the carrier-flow response induced by the collective rise of the bubble swarm, where the bubble contours are superimposed to a 2D map of the instantaneous velocity field. Starting from an initially quiescent liquid, the motion transitions from a collection of largely isolated bubble wakes to a strongly interacting regime in which wake–wake interactions, repeated near-contact events, and interface deformations generate intense shear layers and spatially intermittent high-velocity patches throughout the domain. As time progresses, these fluctuations become increasingly disordered and space-filling, revealing the onset of a turbulent-like, chaotic flow field sustained by buoyancy-driven deformable bubbles (often referred to as *pseudo-turbulence* Alméras *et al.* (2017); Van Wijngaarden (1998); Mercado *et al.* (2010); Hosokawa & Tomiyama (2013)). To provide a first quantitative indicator of the turbulence-like agitation suggested by the flow snapshots in Fig. 7, Fig. 8

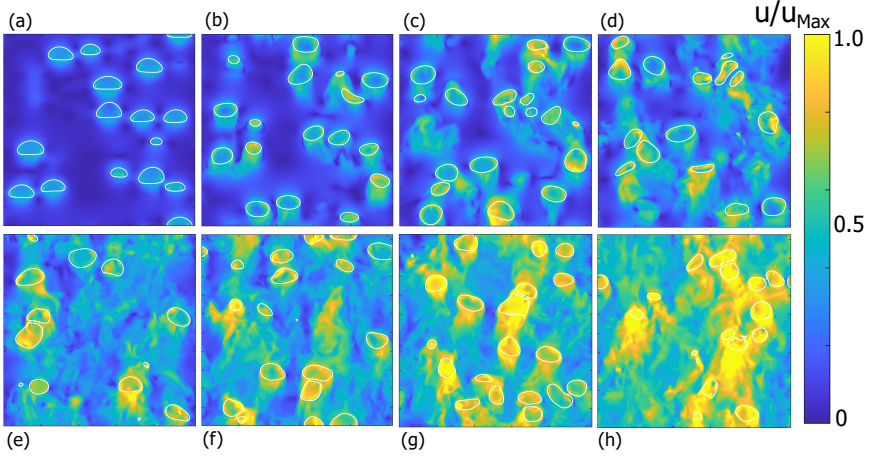


Figure 7: Evolution of the velocity field for the swarm of bubbles in Figure 6, shown as two-dimensional maps of the normalized velocity magnitude u/u_{max} on a mid-plane slice at representative times, with bubble contours superimposed.

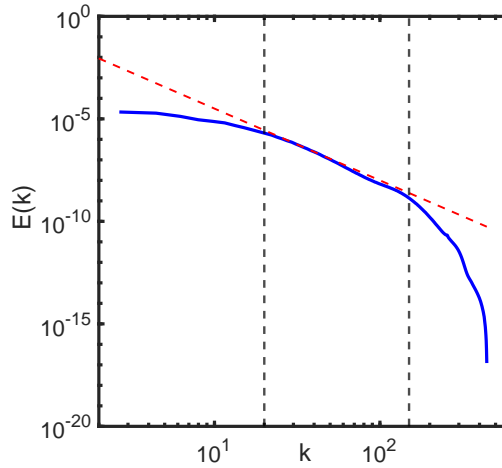


Figure 8: Spectrum of the turbulent kinetic energy (blue line) vs k^{-3} power law

reports the isotropic spectrum of turbulent kinetic energy $E(k)$ of the carrier-phase velocity fluctuations, compared against a k^{-3} reference scaling (dashed line). Over an intermediate band of wavenumbers (delimited by the vertical dashed lines), the spectrum develops a clear power-law decay close to k^{-3} , a hallmark scaling frequently reported in bubble-driven pseudo-turbulence and commonly associated with wake-dominated dynamics at scales at and below the bubble size (i.e. for $k \gtrsim k_b \sim 2\pi/d_b$). At the largest scales (small k), deviations from the reference slope reflect the finite domain size and the anisotropic nature of buoyancy-driven forcing, whereas at high wavenumbers the spectrum steepens due to viscous dissipation and finite-resolution effects.

A dedicated, quantitative characterization of the resulting pseudo-turbulent regime (e.g. energy spectra, anisotropy and intermittency, and scale-by-scale budgets) is deferred to future work.

4. Conclusions

In this work, we have introduced a near-contact interaction (NCI) model for conservative Allen–Cahn phase-field lattice Boltzmann simulations of multiphase flows. The central objective was to provide a physically grounded and computationally efficient mechanism to prevent spurious coalescence in situations where the outcome of interface interaction is controlled by an unresolved thin intervening film. The proposed formulation augments the momentum equation with a short-range repulsive contribution that activates only when two diffuse interfaces approach each other with opposite orientations, thereby mimicking the stabilizing action of unresolved thin-film physics within a mesoscopic diffuse-interface framework.

A distinctive feature of the present approach is that the film thickness is not obtained by ray tracing or geometric reconstruction along interface normals, but is instead estimated analytically from the local phase-field overlap through the equilibrium hyperbolic-tangent profile. This construction preserves locality, improves symmetry of the interaction, and is particularly well-suited for massively parallel GPU-oriented implementations. In combination with the thread-safe recursive-regularized lattice Boltzmann solver and the conservative Allen–Cahn transport equation, the resulting framework remains fully local, scalable, and robust even in the presence of strong density and viscosity contrasts.

The numerical results show that the model captures the correct non-coalescing outcome in droplet-collision benchmarks, including both head-on and off-axis impacts, with excellent agreement against experimental observations. Beyond reproducing the interface kinematics, the simulations recover the expected thin-film hydrodynamic signatures associated with rebound, including suppression and inversion of the film-normal flow and the emergence of stagnation-like regions near the interaction zone. These results indicate that the NCI does not merely act as an artificial penalty, but reproduces the hydrodynamic conditions required for sustained interfacial separation and bounce.

An additional important outcome is the evidence of a self-tuning behavior of the repulsive interaction. Once the repulsive amplitude exceeds the threshold required to avoid coalescence, further increases produce little change in the macroscopic collision dynamics. The analysis of force balances within the activated film region shows that the repulsive contribution remains of the same order as the capillary forcing, while the model adapts predominantly through the spatial support of the activated near-contact region rather than through unbounded local force amplification. This property is particularly appealing because it reduces the sensitivity of the macroscopic dynamics to parameter tuning and suggests that the model behaves as an adaptive near-contact barrier rather than as a stiff numerical constraint.

Finally, the rising-bubble-swarm simulations demonstrate that the method extends naturally to dense many-body configurations in three dimensions, where repeated close approaches and collective rearrangements occur over long integration times. In this regime, the framework preserves bubble identity, avoids spurious topology changes, and sustains complex pseudo-turbulent carrier-phase agitation, thereby opening the way to systematic studies of dense bubbly flows, emulsions, and other strongly interacting disperse systems.

Overall, the present results indicate that the proposed LB-Allen-Cahn-NCI framework provides an effective compromise between physical fidelity, numerical robustness, and computational efficiency for unresolved near-contact dynamics in diffuse-interface multiphase simulations. Future work will focus on a more quantitative calibration of the repulsive closure against thin-film drainage theory and experiments, on extensions to wetting and wall-mediated near-contact events, and on the application of the method to turbulent many-body flows where collisions, rebounds, and topology preservation play a central role on the resulting complex dynamics.

Acknowledgements

A.M. and M.L. acknowledge fundings from the Italian Government through the PRIN (Progetti di Rilevante Interesse Nazionale) Grant (MOBIOS) ID: 2022N4ZNH3 -CUP: F53C24001000006 and computational support of CINECA through the IS CRA B project MIPLAST (IsB31, HP10BZY7BK). S.S. acknowledges the support from the European Research Council under the ERC PoC Grant No. 101187935 (LBFAST). M.L. acknowledges the support of the Italian National Group for Mathematical Physics (GNFM-INdAM).

Declaration of Interests

The authors report no conflict of interest.

REFERENCES

- ALMÉRAS, ELISE, MATHAI, VARGHESE, LOHSE, DETLEF & SUN, CHAO 2017 Experimental investigation of the turbulence induced by a bubble swarm rising within incident turbulence. *Journal of fluid mechanics* **825**, 1091–1112.
- BALACHANDAR, S & EATON, JOHN K 2010 Turbulent dispersed multiphase flow. *Annual review of fluid mechanics* **42** (1), 111–133.
- BENZI, ROBERTO, SUCCI, SAURO & VERGASSOLA, MASSIMO 1992 The lattice boltzmann equation: theory and applications. *Physics Reports* **222** (3), 145–197.
- BERGERON, VANCE 1999 Forces and structure in thin liquid soap films. *Journal of Physics: Condensed Matter* **11** (19), R215–R238.
- BOGDAN, MICHA L, MONTESSORI, ANDREA, TIRIBOCCHI, ADRIANO, BONACCORSO, FABIO, LAURICELLA, MARCO, JURKIEWICZ, LEON, SUCCI, SAURO & GUZOWSKI, JAN 2022 Stochastic jetting and dripping in confined soft granular flows. *Physical Review Letters* **128** (12), 128001.
- BOINOVICH, LB & EMELYANENKO, AM 2002 Forces due to dynamic structure in thin liquid films. *Advances in colloid and interface science* **96** (1-3), 37–58.
- CHIU, PAO-HSIUNG & LIN, YAN-TING 2011 A conservative phase field method for solving incompressible two-phase flows. *Journal of Computational Physics* **230** (1), 185–204.
- CRASTER, RICHARD V & MATAR, OMAR K 2009 Dynamics and stability of thin liquid films. *Reviews of modern physics* **81** (3), 1131–1198.
- DAI, BING, LEAL, L GARY & REDONDO, ANTONIO 2008 Disjoining pressure for nonuniform thin films. *Physical Review E—Statistical, Nonlinear, and Soft Matter Physics* **78** (6), 061602.
- FAKHARI, ABBAS, MITCHELL, TRAVIS, LEONARDI, CHRISTOPHER & BOLSTER, DIOGO 2017 Improved locality of the phase-field lattice-boltzmann model for immiscible fluids at high density ratios. *Physical Review E* **96** (5), 053301.
- GUHA, ABHIJIT 2008 Transport and deposition of particles in turbulent and laminar flow. *Annu. Rev. Fluid Mech.* **40** (1), 311–341.
- GUNN, R. 1965 Characteristics of freely falling water drops: With the use of new apparatus, collisions have been photographed and classified into five basic types. *J. Sci.* **150**, 695–701.
- GUO, ZHAOLI, ZHENG, CHUGUANG & SHI, BAOCHANG 2002 Discrete lattice effects on the forcing term in the lattice boltzmann method. *Physical review E* **65** (4), 046308.
- HÅKANSSON, ANDREAS 2019 Emulsion formation by homogenization: Current understanding and future perspectives. *Annual review of food science and technology* **10** (1), 239–258.
- HOSOKAWA, SHIGEO & TOMIYAMA, AKIO 2013 Bubble-induced pseudo turbulence in laminar pipe flows. *International journal of heat and fluid flow* **40**, 97–105.
- HUANG, K. L. & PAN, K. L. 2021 Transitions of bouncing and coalescence in binary droplet collisions. *J. Fluid Mech.* **928**, A7.
- JACQMIN, DAVID 1999 Calculation of two-phase navier–stokes flows using phase-field modeling. *Journal of computational physics* **155** (1), 96–127.
- JEONG, DARAE & KIM, JUNSEOK 2017 Conservative allen–cahn–navier–stokes system for incompressible two-phase fluid flows. *Computers & Fluids* **156**, 239–246.
- KHARANGATE, CHIRAG R & MUDAWAR, ISSAM 2017 Review of computational studies on boiling and condensation. *International Journal of Heat and Mass Transfer* **108**, 1164–1196.

- KRÜGER, TIMM, KUSUMAATMAJA, HALIM, KUZMIN, ALEXANDR, SHARDT, OREST, SILVA, GONCALO & VIGGEN, ERLAND MAGNUS 2017 *The lattice Boltzmann method*, vol. 10. Springer.
- KRÜGER, TIMM, VARNIK, FATHOLLAH & RAABE, DIERK 2009 Shear stress in lattice boltzmann simulations. *Physical Review E—Statistical, Nonlinear, and Soft Matter Physics* **79** (4), 046704.
- LAURICELLA, MARCO, MUKHERJEE, ARITRA, BRANDT, LUCA, SUCCI, SAURO, IZBASSAROV, DAULET & MONTESSORI, ANDREA 2025a acclb: A high-performance lattice boltzmann code for multiphase turbulence on multi-gpu architectures. *Procedia Computer Science* **267**, 40–51.
- LAURICELLA, MARCO, TIRIBOCCHI, ADRIANO, SUCCI, SAURO, BRANDT, LUCA, MUKHERJEE, ARITRA, LA ROCCA, MICHELE & MONTESSORI, ANDREA 2025b Thread-safe multiphase lattice boltzmann model for droplet and bubble dynamics at high density and viscosity contrasts. *Physics of Fluids* **37** (7).
- LI, JIE 2016 Macroscopic model for head-on binary droplet collisions in a gaseous medium. *Physical review letters* **117** (21), 214502.
- LIU, DA, HU, YANG, ZHANG, SHITING, ZHU, YUQI, HE, QIANG & LI, DECAI 2025 Phase field-lattice boltzmann model for two-phase flows with near-contact interactions. *Physics of Fluids* **37** (9).
- MALASPINAS, ORESTIS 2015 Increasing stability and accuracy of the lattice boltzmann scheme: recursivity and regularization. *arXiv preprint arXiv:1505.06900*.
- MERCADO, JULIAN MARTINEZ, GOMEZ, DANIEL CHEHATA, VAN GILS, DENNIS, SUN, CHAO & LOHSE, DETLEF 2010 On bubble clustering and energy spectra in pseudo-turbulence. *Journal of fluid mechanics* **650**, 287–306.
- MILLER, CASS T, CHRISTAKOS, GEORGE, IMHOFF, PAUL T, MCBRIDE, JOHN F, PEDIT, JOSEPH A & TRANGENSTEIN, JOHN A 1998 Multiphase flow and transport modeling in heterogeneous porous media: challenges and approaches. *Advances in Water Resources* **21** (2), 77–120.
- MONTESSORI, ANDREA, LA ROCCA, MICHELE, AMATI, GIORGIO, LAURICELLA, MARCO, TIRIBOCCHI, ADRIANO & SUCCI, SAURO 2024 High-order thread-safe lattice boltzmann model for high performance computing turbulent flow simulations. *Physics of Fluids* **36** (3).
- MONTESSORI, ANDREA, LAURICELLA, MARCO, MUKHERJEE, ARITRA & BRANDT, LUCA 2026 Breakdown of kolmogorov scaling and modified energy transfer in bubble-laden turbulence. *Physical Review Fluids* **11** (2), 024605.
- MONTESSORI, ANDREA, LAURICELLA, MARCO, TIRELLI, NICOLA & SUCCI, SAURO 2019 Mesoscale modelling of near-contact interactions for complex flowing interfaces. *Journal of Fluid Mechanics* **872**, 327–347.
- MONTESSORI, A, PRESTININZI, P, LA ROCCA, M & SUCCI, S 2015 Lattice boltzmann approach for complex nonequilibrium flows. *Physical Review E* **92** (4), 043308.
- ORME, MELISSA 1997 Experiments on droplet collisions, bounce, coalescence and disruption. *Progress in Energy and Combustion Science* **23** (1), 65–79.
- PHILIPPI, PAULO CESAR, HEGELE JR, LUIZ ADOLFO, DOS SANTOS, LUIS ORLANDO EMERICH & SURMAS, RODRIGO 2006 From the continuous to the lattice boltzmann equation: The discretization problem and thermal models. *Physical Review E—Statistical, Nonlinear, and Soft Matter Physics* **73** (5), 56702.
- QIAN, J. & LAW, C. K. 1997 Regimes of coalescence and separation in droplet collision. *J. Fluid Mech.* **331**, 59–80.
- RINGROSE, PHILIP S, FURRE, ANNE-KARI, GILFILLAN, STUART MV, KREVROR, SAMUEL, LANDRØ, MARTIN, LESLIE, RORY, MECKEL, TIP, NAZARIAN, BAMSHAD & ZAHID, ADEEL 2021 Storage of carbon dioxide in saline aquifers: physicochemical processes, key constraints, and scale-up potential. *Annual review of chemical and biomolecular engineering* **12**, 471–494.
- RISSE, FRÉDÉRIC 2018 Agitation, mixing, and transfers induced by bubbles. *Annual Review of Fluid Mechanics* **50**, 25–48.
- SATTARI, AMIRMOHAMMAD, HANAFIZADEH, PEDRAM & HOORFAR, MINA 2020 Multiphase flow in microfluidics: From droplets and bubbles to the encapsulated structures. *Advances in Colloid and Interface Science* **282**, 102208.
- SHAN, XIAOWEN 2006 Analysis and reduction of the spurious current in a class of multiphase lattice boltzmann models. *Physical Review E—Statistical, Nonlinear, and Soft Matter Physics* **73** (4), 047701.
- SHAW, RAYMOND A 2003 Particle-turbulence interactions in atmospheric clouds. *Annual Review of Fluid Mechanics* **35** (1), 183–227.

- SUBRAMANIAM, SHANKAR 2020 Multiphase flows: Rich physics, challenging theory, and big simulations. *Physical Review Fluids* **5** (11), 110520.
- SUCCI, SAURO 2018 *The lattice Boltzmann equation: for complex states of flowing matter*. Oxford university press.
- SUCCI, SAURO, AMATI, GIORGIO, BERNASCHI, MASSIMO, FALCUCCI, GIACOMO, LAURICELLA, MARCO & MONTESSORI, ANDREA 2019 Towards exascale lattice boltzmann computing. *Computers & Fluids* **181**, 107–115.
- SZEG, GABOR 1939 *Orthogonal polynomials*, , vol. 23. American Mathematical Soc.
- THAMPI, S. P., ANSUMALI, S., ADHIKARI, R. & SUCCI, S. 2013 Isotropic discrete laplacian operators from lattice hydrodynamics. *Journal of Computational Physics* **234**, 1–7.
- TIRIBOCCHI, ADRIANO, DURVE, MIHIR, LAURICELLA, MARCO, MONTESSORI, ANDREA, TUCNY, JEAN-MICHEL & SUCCI, SAURO 2025 Lattice boltzmann simulations for soft flowing matter. *Physics Reports* **1105**, 1–52.
- TIRUMKUDULU, MAHESH S & RUSSEL, WILLIAM B 2004 Role of capillary stresses in film formation. *Langmuir* **20** (7), 2947–2961.
- VAN WIJNGAARDEN, L 1998 On pseudo turbulence. *Theoretical and computational fluid dynamics* **10** (1), 449–458.
- ZU, YQ & HE, SHUISHENG 2013 Phase-field-based lattice boltzmann model for incompressible binary fluid systems with density and viscosity contrasts. *Physical Review E—Statistical, Nonlinear, and Soft Matter Physics* **87** (4), 043301.